International Journal of Solids and Structures 161 (2019) 96–110

Contents lists available at ScienceDirect

International Journal of Solids and Structures

journal homepage: www.elsevier.com/locate/ijsolstr

An isotropic self-consistent homogenization scheme for chemo-mechanical healing driven by pressure solution in halite

Xianda Shen*, Chloé Arson

School of Civil and Environmental Engineering, Georgia Institute of Technology, USA

A R T I C L E I N F O

Article history:
Received 3 February 2018
Revised 25 June 2018
Available online 9 November 2018

Keywords:
Mechanical healing
Pressure solution
Homogenization
Self-consistent scheme
Chemo-mechanical couplings
Creep

A B S T R A C T

Mechanical healing is the process by which a damaged material recovers mechanical stiffness and strength. Pressure solution is a very effective healing mechanism, common in crystalline media. Chemical reactions initiate at the location of microstructure defects, which would be very difficult to account for in a homogenization scheme that separates the solid and the pore phases, as is classically the case. Here, we propose a novel chemo-mechanical homogenization model in which the inclusion is not a grain, but rather, a space that contains a pore and discontinuities, where chemical processes take place. Mass and energy balance equations are rigorously established to predict the chemical eigenstrain of each inclusion, which, added to the elastic deformation, provides the microstrain of each inclusion. From there, Hill's inclusion-matrix interaction law is used to upscale strains and stresses at the scale of a Representative Elementary Volume (REV). The model was calibrated against experimental results published in the literature for salt rock. Subsequent sensitivity analyses show that in samples with same porosity but with inclusions that have different initial void sizes, inclusions with larger voids have a negligible healing rate and they are slowing down the overall healing rate of the REV. The highest healing rate is reached in samples with uniformly distributed void sizes. In addition, the healing rate increases with the initial porosity, but the final porosity change does not depend on the initial porosity of the sample. Principal stresses of higher magnitude are noted in the inclusions that are part of REVs of high initial porosity. In specimens with smaller inclusions (i.e., smaller grains), principal stresses are more widely distributed in magnitude and the healing rate is higher. The proposed homogenization method paves the way to many future developments for upscaling chemo-mechanical processes in heterogeneous media, and can be used to design self-healing materials.

1. Introduction

Self-healing materials gained interest in recent years, due to their long term performance (Gardner et al., 2014; Zhu and Arson, 2015; Davies and Jefferson, 2017). Healing, the process by which a damaged material recovers mechanical stiffness and strength, can be due to different mechanisms. Voyiadjis et al. (2011) distinguished active systems, which are coupled with damage mechanisms (Barbero et al., 2005; White et al., 2001) and passive systems, which are triggered by external stimulations (Li and Uppu, 2010). Thermodynamics principles were applied to establish self-healing models for crushed salt rock (Miao et al., 1995), thermoset polymers (Mergheim and Steinmann, 2013) and shape memory polymers (Voyiadjis et al., 2012). A micro-damage fatigue and healing model was also proposed for asphalt mixes; the formulation is based on coupled nonlinear viscoelastic, viscoplastic, and viscodamage constitutive equations (Al-Rub et al., 2010).

Pressure solution is a very effective healing mechanism, common in crystalline media: dissolution occurs at the grain-to-grain contacts that are under high stress, ions are transported by diffusion in fluid films at grain boundaries, and re-precipitate at grain-to-grain contacts that are under low stress. Diffusion can happen within the lattice of crystals, e.g. Nabarro–Herring creep, or along the grain boundaries, e.g. Coble creep (Wheeler, 2010; McCLAY, 1977). The presence of inter-granular brine enhances pressure solution and accelerates creep and healing rates (Paterson, 1973; Rutter and Elliott, 1976; Raj, 1982; Rutter, 1983; Lehner, 1995). In damp halite (salt rock), pressure solution is the dominating creep mechanism for temperatures below 350 °C, as shown in Fig. 1. Crystal slip plasticity and grain boundary sliding are two other important densification mechanisms in salt, observed under uniaxial loading (Holcomb and Zeuch, 1990; Bourcier et al., 2013). The

---

* Corresponding author.
E-mail addresses: xdshen@gatech.edu (X. Shen), chloe.arson@ce.gatech.edu (C. Arson).

https://doi.org/10.1016/j.ijsolstr.2018.11.010

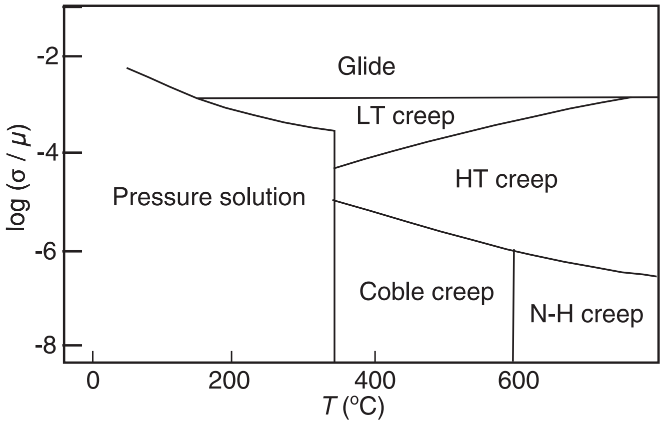

Fig. 1. Deformation map of damp halite. LT, low temperature; HT, high temperature; N-H, Nabarro-Hering. Adapted from Urai et al. (1986).

densification rate is largely influenced by crystallographic orientations, crystal boundary orientations, density, temperature and the loading history. In addition, when salt aggregates are saturated and compacted in brine, the densification rate increases rapidly. Larger effective stress and smaller grain size also lead to rapid creep (Spiers and Brzesowsky, 1993). Under high temperature and large stress, recrystallization can be observed in some highly strained areas, but overall, porosity decreases. During uniaxial creep tests, halite polycrystals become denser and mainly deform because of crystal-to-crystal interactions. In brine-saturated halite polycrystals, deformation is first driven by pressure solution, due to the development of normal stress at the grain contacts. Second, deformation happens because the grain boundaries are lubricated due to the presence of fluid. Third, grain scale cataclasis occurs due to crystal slip plasticity and grain boundary sliding. When the compressive effective stress is less than −4MPa, creep is dominated by pressure solution. When the compressive effective stress is larger than −4MPa (i.e., when the effective stress is less than −4MPa), plastic related mechanisms, such as dislocation, microcracking and recrystallization, have a significant effect on the deformation of the polycrystal. In this tudy, we focus on halite under low compressive stress conditions (i.e., between −4MPa and 0MPa) and at ambient temperature, in which creep is controlled by pressure solution (Fig. 1).

A microphysical model for healing in rocksalt was proposed at the crack scale, taking diffusive mass transfer as the controlling mechanism in the longer term (Houben et al., 2013). Deformation measures were conducted at the contact between polished flat lenses immersed in saturated brine, to understand the fundamental pressure solution mechanisms at halite-halite and halite-silica contacts (Hickman and Evans, 1991). Phenomenological creep models were formulated to account for effective diffusivity, and calibrated against experiments conducted on rocksalt (Spiers et al., 1990; Yang et al., 1999) and calcite (Zhang and Spiers, 2005). A compaction model that distinguishes dissolution, precipitation and diffusion - dominated creep rates was also proposed for anhydrite, assuming a simple cubic packing of spherical grains (Pluymakers and Spiers, 2015).

The mechanical behavior of more diverse and realistic microstructures can be predicted by homogenization, i.e. by upscaling crystal-, crack- or grain- scale mechanisms to the scale of a Representative Elementary Volume (REV). Eshelby's theory (Eshelby, 1957) allows calculating the REV stress and strain fields based on the knowledge of the stress and strain fields of "inclusions" embedded in a "matrix". In the dilute scheme, the inclusions do not interact with each other and the macroscopic stress and strain fields can be obtained by volumetric average. In Mori–Tanaka scheme, the stiffness tensor of the REV is deduced from the micro/macro interaction law that relates the REV stress and strain fields to the inclusion stress and strain fields, in which the mechanical properties of the matrix are given. Mori-Tanaka's scheme allows predicting explicitly the effective properties of composite materials (Mori and Tanaka, 1973). However, if the composite material contains inclusions with different orientations and shapes, the predicted stiffness tensor may violate symmetry requirements (Benveniste, 1987; Castañeda and Willis, 1995). The self-consistent method assumes that there is no dominating phase in the medium, so that the matrix around each inclusion (or crystal) is made of all the inclusions (or crystals) that surround that inclusion. The self-consistent method provides an accurate but implicit solution to the homogenization problem, particularly suitable for polycrystals (Hill, 1965). Self-consistent homogenization models were proposed for elastic-plastic materials (Kröner, 1961), viscoplastic materials (Weng, 1982) and polycrystals subject to anisotropic damage (Pouya et al., 2017). Asymptotic expansions were introduced in a homogenization scheme to formulate a macroscopic model of compacted swelling clays and to correlate macroscopic parameters with microscopic electro-hydrodynamics (Moyne and Murad, 2002). Multi-scale homogenization schemes were also employed to predict stiffness changes induced by mineral dissolution in calcite (Arson and Vanorio, 2015). However, no homogenization scheme was proposed to date to couple chemical and mechanical microstructure changes in a self-consistent micro/macro model and to predict the mechanical behavior of self-healing materials.

We thus formulate a chemo-mechanical homogenization model to predict time-dependent healing processes in halite, which we consider as a model geomaterial. In Section 2, we present the thermodynamic and constitutive equations that govern pressure solution at the scale of an inclusion, made of eight grain fractions and containing a pore located at the intersection of three orthogonal grain-to-grain contact planes. We explain Hill's self-consistent homogenization scheme in Section 3. The model is calibrated against published results of oedometer tests (i.e., tests in which salt samples were subjected to a vertical compression controlled in displacement at the top boundary, with fixed displacements at the bottom and lateral boundaries). Results are presented in Section 4. In Section 5, we analyze the sensitivity of the model to inclusion size (i.e., grain size), initial porosity, void size distribution and inclusion orientation.

2. Microscopic chemo-mechanical model

2.1. Pressure solution theory

When subjected to normal stress, salt crystals (also called grains in the following) dissolve at contacts. Ions diffuse along fluid films at crystals' boundaries and precipitate on pore walls. In the following, the plane that contains the axes x and y (respectively y and z, x and z) is noted XY (respectively YZ, XZ). Fig. 2 illustrates the pressure solution phenomenon around a pore, in plane XY. In that plane, the pore is surrounded by four grains. Grain dissolution at the contacts results in a size reduction of the grains (δx and δy in Fig. 2). Salt ions then diffuse along contact planes that are normal to the dissolution planes, i.e., in plane XY. Ions finally precipitate at the pore wall, because pore fluid pressure is lower in the pore than at the grain contacts.

In brine-saturated specimens, dissolution, diffusion and precipitation happen simultaneously (but at different locations). Let us analyze the thermodynamic processes that govern pressure solution at one grain contact. We assume that flat grain edges that are "in contact" are in fact separated by a thin fluid film (Rutter, 1983; Pluymakers and Spiers, 2015). The assumed geom-

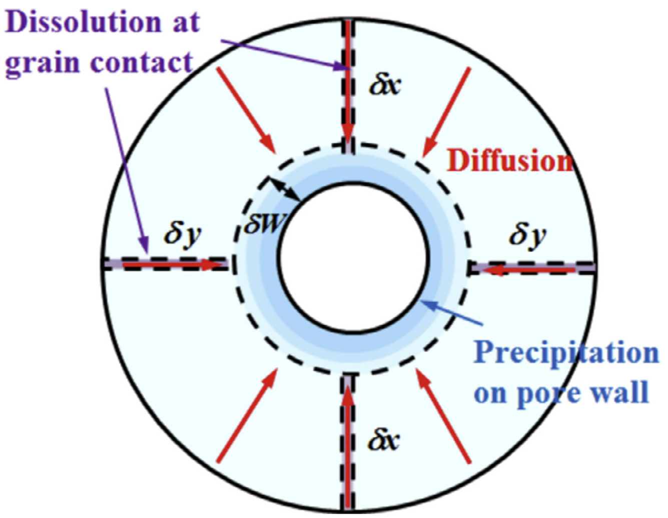

Fig. 2. Mass transfer induced by pressure solution around a pore, in contact plane XY.

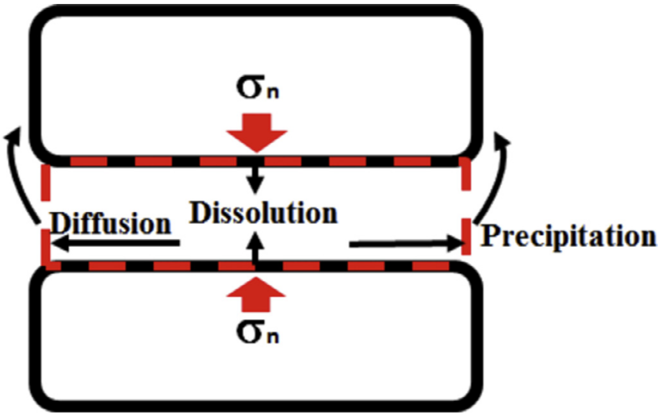

Fig. 3. Pressure solution mechanisms at a grain-to-grain contact (plane XZ).

etry of the contact is shown in Fig. 2 (plane XY) and Fig. 3 (plane XZ).

Locally (i.e. at the grain scale), an increase of normal effective stress in the solid skeleton changes the difference of chemical potential ($\triangle\mu$) of the solid constituent of the halite REV in reference to the solute (brine in this case). We have:

$$\triangle\mu \approx (\sigma_n - P_f)\Omega \tag{1}$$

where σ_n is the normal stress at the grain contact (averaged on the surface of the contact), P_f is the pore fluid pressure, and Ω is the molar volume. The change of chemical potential of the solute can be expressed as a function of the mineral concentration:

$$\triangle\mu \approx R^*T\ln\left(\frac{C}{C_o}\right) \tag{2}$$

where C is the concentration of minerals (ions) in the fluid, C_o is the solubility of the solid at the pore walls - assumed to be uniform because the fluid pressure in the pores can be assumed uniform under low stress. R^* is the gas constant and T is the Kelvin temperature (Spiers et al., 2003). Assuming a linear dissolution law, common for halite (Brantley et al., 2008), the expression of the dissolution velocity V_c at the contacts (i.e., at grain scale) is (van Noort and Spiers, 2009):

$$V_c = \alpha k_+ \Omega \frac{\triangle C}{C_o} \tag{3}$$

where α is a parameter describing the influence of the topology of the grain boundary on the pressure solution rate, k_+ is the unstressed mineral dissolution rate, which is constant under the pore fluid pressure. α varies from 0 to 1, based on stress concentrations, porosity and grain boundary. Pluymakers (2015) suggested $\alpha \approx 0.9$ for dissolution controlled pressure solution and α=1 for precipitation controlled pressure solution, with the assumption that the precipitation rate is not influenced by the structure of the grain boundary. At a given contact, dissolution, diffusion and precipitation processes are serial, thus the dissolution velocity at grain contacts is controlled by the slowest of these processes. The expressions for dissolution controlled interface dissolution velocity V_s and precipitation controlled interface dissolution velocity V_p are obtained from Eqs. (1)–(3), as follows:

$$V_s = \alpha_s k_+ \Omega\left[\exp\left(\frac{\sigma_n^e \Omega d_s^2}{R^* T a_c}\right) - 1\right] \tag{4}$$

$$V_p = \alpha_p k_+ \Omega\left[\exp\left(\frac{\sigma_n^e \Omega d_s^2}{R^* T a_c}\right) - 1\right] f(\phi^*) \tag{5}$$

where σ_n^e is the effective stress on the grain boundary, d_s is the diameter of the grain, a_c is the contact area. $f(\phi^*)$ is a function of the porosity ϕ^* and of the initial porosity ϕ_o^*. Based on the equation of mass conservation, $f(\phi^*)$ is equal to $\phi^*/(\phi_o^* - \phi^*)$ (Pluymakers and Spiers, 2015). Note: Eqs. (4) and (5) are stated here for reference, but not used in the model, because the kinematics of pressure solution in halite is actually governed by diffusion. In the following, we detail the balance equations that result from a dissipation of energy due to the diffusion of dissolved ions. The interested reader is referred to van Noort and Spiers (2009); Pluymakers and Spiers (2015) for the full derivations of the geometrical terms involved in Eqs. (4) and (5).

2.2. Hollow sphere inclusion model

We upscale the grain-scale pressure solution model to the laboratory sample scale by homogenization. We use a self-consistent scheme, in which inclusions are spherical composites, made of a spherical pore that lies at the intersection between three orthogonal grain contact planes. Admittedly, the assumption of spherical inclusions is a limitation of the model. During the creep process, it is expected that inclusions change shape over time. However, it has to be noted that the local strain of each inclusion is calculated at each time step, which allows accounting for inclusion shape changes in the overall mechanical response predicted at the scale of the REV. The inclusion considered here thus contains a pore and 8 grain fractions, see Fig. 4. Noting r_g the radius of the hollow spherical inclusion, W the thickness of the shell around the pore (called wall thickness in the following), and assuming that W is uniform around the pore, the spherical void's diameter is $2r_g - 2W$. Grain contact planes within an inclusion are shown in Fig. 4(b). The REV (Fig. 5) is the volume that contains a representative distribution of inclusion types, which can be defined in terms of inclusion size, pore size, inclusion orientation (or grain contact plane orientation).

At the inclusion scale, under normal stress, the solid mineral is dissolved at contact planes, the solute diffuses along the contact planes towards the pore inside the inclusion, and precipitates at the pore wall. Let us consider one pair of contact planes. A fluid film of thickness S lies between these two planes. The shape of the interface pore/film is an annulus of area A_{ew}, where A_{ew} is the product of S by the perimeter of the pore wall, noted $P(w)$. Due to mass conservation principles, the mass of mineral that diffuses radially from the contact plane towards the pore inside the inclusion, through the annulus of area A_{ew}, is equal to the mass of mineral that is dissolved at the contact plane. The corresponding equation can be written as:

$$J(w)A_{ew} = \frac{2V_c A_{er}}{\Omega} \tag{6}$$

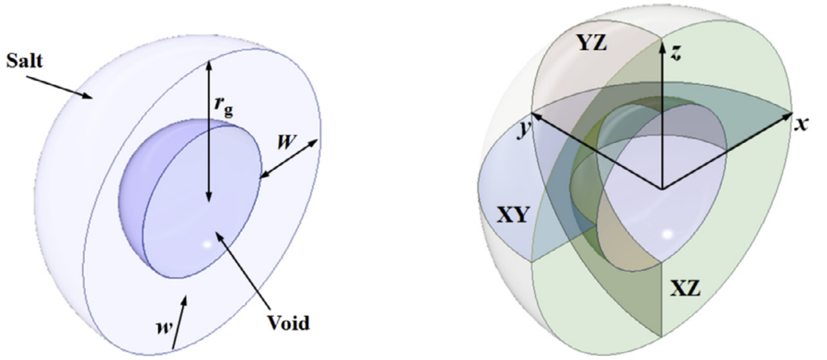

(a) Hollow spherical inclusion

(b) Spherical pore at the intersection between grain contact planes

Fig. 4. Schematic representation of an inclusion.

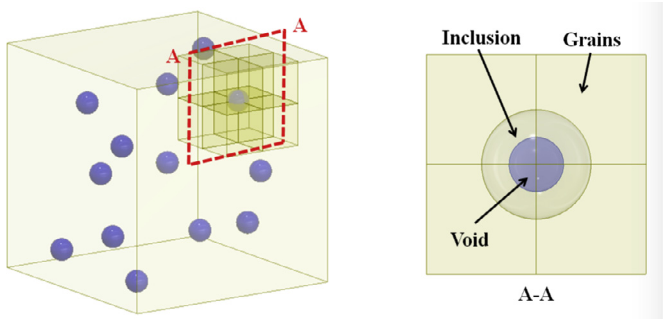

Fig. 5. Schematic representation of the halite REV.

where $J(w)$ is the radial diffusion flux, and A_{er} is the area of the part of the contact plane where dissolution occurs, between the periphery of the contact surface and the dissolution front located at a distance $w \leq W$ from the periphery (where W is the pore wall thickness). The dissolution surface has the shape of a ring. Its area is the difference between the area of the cross section of the inclusion, $\pi(r_g)^2$, and that of the sphere delimited by the dissolution front, $\pi(r_g - w)^2$. Thus we have: $A_{er} = (2r_g w - w^2)\pi$.

Differentiating Eq. (2) with respect to C yields $\partial\mu/\partial C = R^*T/C$. Moreover, the radial diffusion flux $J(w)$ is related to the chemical potential μ according to Fick's first law:

$$J(w) = -D\frac{\partial C}{\partial w} = -\frac{DC(w)}{R^*T}\frac{\partial \mu}{\partial w} \tag{7}$$

where D is the grain boundary diffusion coefficient. The energy dissipation per unit volume, noted $\dot{\Delta}_w$, is equal to $-J(w)\partial\mu/\partial w$ (Lehner, 1990). The radial energy dissipation increment is thus:

$$d\dot{\Delta}_w = -J(w)\frac{\partial \mu}{\partial w}SP(w)dw \tag{8}$$

Under low stress conditions, we assume that the solute concentration $C(w)$ along the grain boundary is equal to that in the pore, C_o (Rutter, 1983; Schutjens and Spiers, 1999; Pluymakers and Spiers, 2015). Integrating the radial energy dissipation increment over the distance that goes from a point at the periphery of the inclusion to the pore wall, and using both Eqs. (6) and (7), we obtain the expression of the total dissipation $\dot{\Delta}_t^{XY}$ on a contact plane, as follows:

$$\dot{\Delta}_t^{XY} = \int_0^W \frac{2R^*T{V_c^{XY}}^2\pi(2r_g w - w^2)^2}{DC_o S\Omega^2(r_g - w)}dw \tag{9}$$

where we took the contact plane XY as an example. V_c^{XY} is the velocity of the dissolution that occurs on plane XY and leads to a deformation along the z-axis. Both grains in contact dissolve, so the overall dissolution rate at the contact is $2V_c^{XY}$. During one unit of time, the work of the compressive force that acts on plane XY to produce a vertical displacement of $2V_c^{XY}$ is the product of $2V_c^{XY}$ by the normal effective stress on plane XY (noted σ_n^{eXY}) and by the area of the contact surface in plane XY, $A_{er} = (2r_g W - W^2)\pi$. Assuming that the inclusion work input is entirely dissipated by pressure solution, the total dissipation can thus be expressed as:

$$\dot{\Delta}_t^{XY} = 2\sigma_n^{eXY}V_c^{XY}(2r_g W - W^2)\pi \tag{10}$$

Substituting Eq. (9) into Eq. (10), the dissolution velocity normal to the contact plane XY is expressed as:

$$V_c^{XY} = \frac{DSC_o\Omega^2\sigma_n^{eXY}\left(2r_g W - W^2\right)}{R^*T\int_o^W \frac{\left(2r_g w - w^2\right)^2}{r_g - w}dw} \tag{11}$$

The rate of mineral volume dissolved, $\dot{V}_{XY}$, depends on the dissolution velocity on plane XY and on the area of the contact surface: $\dot{V}_{XY} = (2r_g W - W^2)\pi V_c^{XY}$. The dissolution velocity and the rate of volume dissolved on planes YZ and XZ can be obtained in the same way. The chemical viscous strain rate $\dot{\epsilon}_x$, $\dot{\epsilon}_y$ and $\dot{\epsilon}_z$ are obtained from the dissolution velocity on planes YZ, plane XZ and plane XY respectively, as follows:

$$\dot{\epsilon}_x = V_c^{YZ}/r_g \tag{12}$$

$$\dot{\epsilon}_y = V_c^{XZ}/r_g \tag{13}$$

$$\dot{\epsilon}_z = V_c^{XY}/r_g \tag{14}$$

The mineral only dissolves on the contact planes. In addition, we assume that the mineral precipitates on the pore wall uniformly. Thus, the change of thickness δW^i at time step t_i can be calculated from the total volume of mineral dissolved and from the pore's surface area A_s^{i-1} at time step t_{i-1}. Diffusion and precipitation processes are illustrated for plane XY in Fig. 2. We finally obtain:

$$\delta W^i = \frac{\dot{V}_{XY}^i + \dot{V}_{YZ}^i + \dot{V}_{XZ}^i}{A_s^{i-1}}\delta t \tag{15}$$

where δt is the time step.

We simulate an isotropic creep test at the inclusion scale. The inclusion size and the chemical parameters used in the simulations are listed in Table 1. The inclusion is subjected to a hydrostatic stress of −1 MPa, −2 MPa and −3 MPa, and we follow the evolution of the inclusion geometry in each case. Simulation results are presented in Fig. 6.

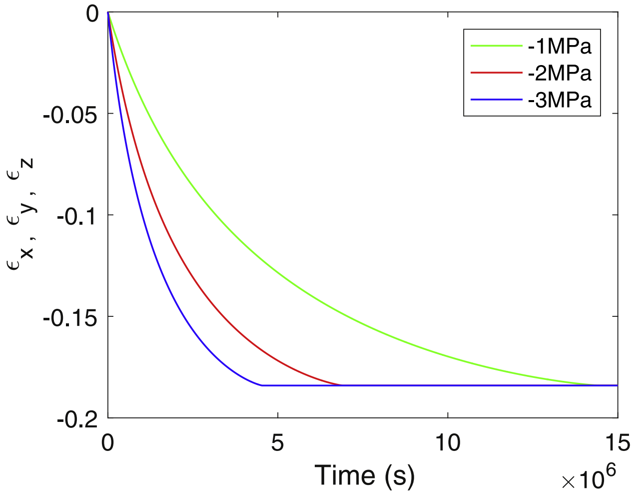

(a) ϵ_x‘ϵ_y‘ϵ_z vs. time

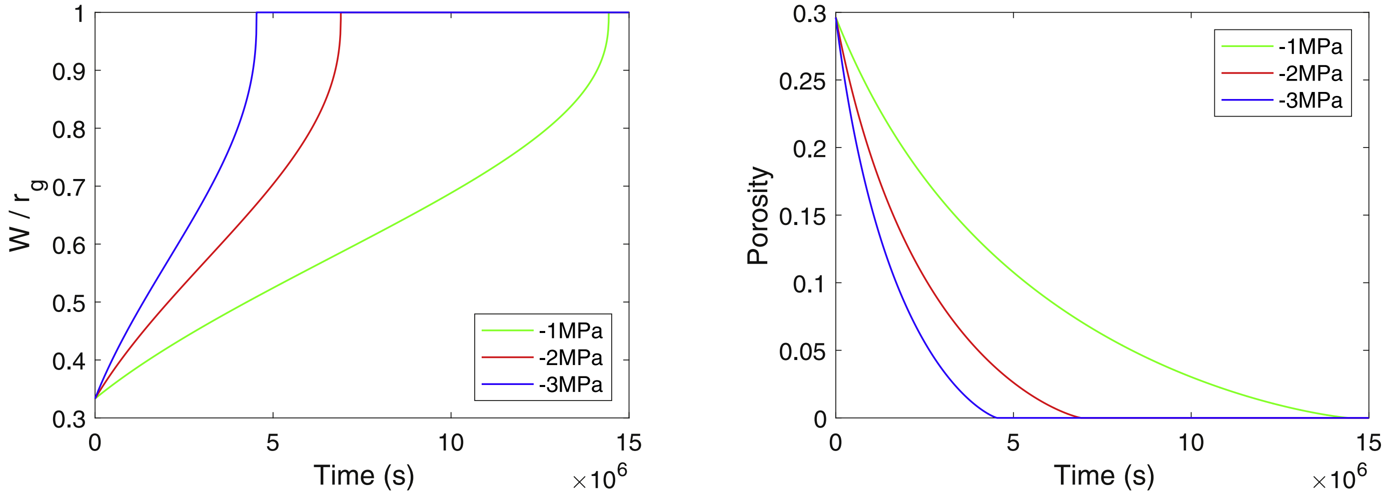

(b) $W \triangleleft r_g$ vs. time (c) porosity vs. time

Fig. 6. Evolution of the inclusion geometry during an isotropic creep test.

Table 1
Inclusion parameters in the isotropic and uniaxial creep tests.

Initial size		Chemical property		
r_g *mm*	W_o *mm*	*DS* mm^3/s	*C* mol/mm^3	Ω mm^3/mol
0.15	0.05	1×10^{-8}	6.48×10^{-6}	2.7×10^4

Isotropic compressive stress induces dissolution at each contact plane, therefore $\epsilon_x = \epsilon_y = \epsilon_z < 0$. Precipitation at the pore wall stops when the wall thickness becomes equal to the radius of the inclusion: the pore is then fully filled with precipitated solid mineral, i.e. the inclusion is fully healed. When precipitation stops, deformation components reach a plateau. Fig. 6(a) reflects this process and confirm that the healing rate increases with the magnitude of the external stress imposed during the creep test. The time to achieve full inclusion healing is 1.4431×10^7 s (107 days), 6.9039×10^6 s (80 days) and 4.5374×10^6 s (52 days), under -1MPa, -2MPa and -3MPa, respectively. Since precipitation is assumed to be uniform on the pore wall, the geometry of the fully healed inclusion is determined by the initial dimensions of the inclusion rather than by the external stress conditions. According to Eq. (11), the relationship between the healing rate and the stress is not linear. The results show that, as expected, the healing rate is influenced by the area of the contact (term W^2 in (11)). The rate of porosity change decreases over time, as expected (Fig. 6(c)).

In order to study healing-induced anisotropy, we now simulate uniaxial creep tests for various inclusion orientations, defined by three angles ψ (coordinates x′y′z′), θ (coordinates x′′y′′z′′) and ϕ (coordinates x′′′y′′′z′′′), as shown in Fig. 7. Due to the symmetry of the loading under uniaxial stress conditions, ψ has no influence on the deformation of the inclusion. Due to the symmetries of the spherical inclusion, we only simulate cases where θ and ϕ are between 0° to 45°. In total, 13 cases were simulated (Figs. 8 and 9).

For non-zero values of ϕ and θ, the dissolution rate in planes YZ and XZ increases with θ (leading to an increase of $\dot{\epsilon}_x$ and $\dot{\epsilon}_y$ respectively). For a given non-zero value of θ, increasing ϕ increases the dissolution rate in plane XZ (leading to an increase

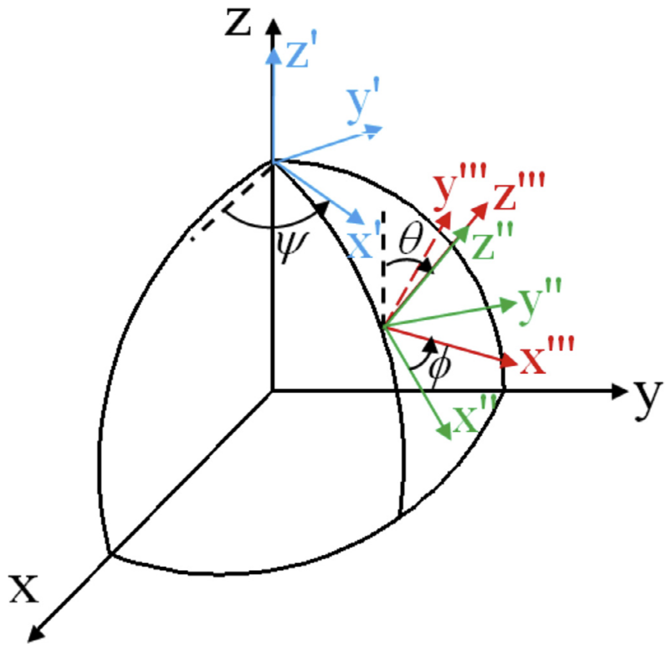

Fig. 7. Angular coordinates adopted to define the orientation of the inclusion relative to the loading axis.

of $\dot{\epsilon}_y$) and decreases the dissolution rate in plane YZ (leading to a decrease of $\dot{\epsilon}_x$). Fig. 8(b) shows the eolution of ϵ_x. The evolution of ϵ_y, not shown here, follows the same trend. For the initial dimensions chosen in this parametric study, Fig. 8(c) shows that the strain rate $\dot{\epsilon}_z$ is controlled by angle θ: $\dot{\epsilon}_z$ reduces when θ increases, which results in a larger value ϵ_z at the final stage, when healing is complete. The angle ϕ does not influence the strain rate $\dot{\epsilon}_z$ significantly. The evolution of the wall thickness (Fig. 9(a)) and of porosity (Fig. 9(b)) confirm that the healing rate increases with the sum of the stresses normal to the contact planes. The trace of the imposed stress does not depend on the inclusion orientation, thus the healing efficiency is the same for all inclusion orientations tested. Simulation results follow the trends expected from the model formulation and are in agreement with classical physical observations, which justifies the upscaling method proposed in the following section.

3. Homogenization scheme

3.1. Averaging method

We consider a REV made of an assembly of hollow spherical inclusions that have the properties described in Section 2. In order to represent the microstructure of a polycrystal such as halite, we assume that there is no dominating phase in the REV composite: each hollow sphere is thought of as an inclusion embedded in a matrix made of all the inclusions present in the REV. Thus, we employ a self-consistent homogenization scheme to determine the relationship between the stress and strain fields of the REV and those of the inclusions. A macroscopic field can be calculated by averaging its microscopic counterpart over the REV. We introduce the solid angle Λ, defined such that $d\Lambda = \sin\theta \mathrm{d}\theta \mathrm{d}\psi$. Noting $p(\psi, \theta, \phi)$ the probability of the occurrence of orientation (ψ, θ, ϕ), the average of a field function f that depends on (ψ, θ, ϕ) is defined as (Pouya et al., 2016):

$$\bar{f} = \frac{1}{\Lambda^*}\int_{\Lambda^*} f(\psi,\theta,\phi)p(\psi,\theta,\phi)\sin\theta \mathrm{d}\psi \mathrm{d}\theta \mathrm{d}\phi$$

$$= \frac{1}{8\pi^2}\int_{\psi=0}^{2\pi}\int_{\theta=0}^{\pi}\int_{\phi=0}^{2\pi} f(\psi,\theta,\phi)p(\psi,\theta,\phi)\sin\theta \mathrm{d}\psi \mathrm{d}\theta \mathrm{d}\phi \quad (16)$$

Because the inclusion model has three pairwise perpendicular axes of symmetry which intersect at a center of symmetry, the domains of variation of θ and ϕ reduce to the interval $[0, \pi/2]$. In transverse symmetric loading conditions (like in isotropic, uniaxial, and oedometer tests), the model is symmetric about the z-axis at the REV scale, so that the rotation by an angle ψ does not influence the mechanical response of the REV. Thus in the following, ψ is set equal to 0, without losing the generality of the model. Eq. (18) is rewritten as:

$$\bar{f} = \frac{2}{\pi}\int_{\theta=0}^{\pi/2}\int_{\phi=0}^{\pi/2} f(\theta,\phi)p(\psi,\theta)\sin\theta \mathrm{d}\theta \mathrm{d}\phi \quad (17)$$

More generally, the average of a field function is calculated as:

$$\bar{f} = \frac{1}{\Lambda^*}\int_{\Lambda^*} f(\psi,\theta,\phi,\nu_1)p(\psi,\theta,\phi)p_1(\nu_1)$$
$$\cdots p_n(\nu_n)\sin\theta \mathrm{d}\psi \mathrm{d}\theta \mathrm{d}\phi \mathrm{d}\nu_1 \cdots \mathrm{d}\nu_n \quad (18)$$

where p_i is the probability of occurrence of the geometric characteristic ν_i in the REV (e.g., inclusion size or porosity). In this paper, we assume that all probability density functions $(p, p_1, \cdots p_n)$ are independent. We derive a close formulation in which we assume that ϕ and θ are uniformly distributed in the interval $[0, \pi/2]$. The model can of course be used for other orientation distributions, depending on available microstructure information.

3.2. Inclusion-matrix interaction model

Hill's self-consistent method (Hill, 1965) is used to upscale the mechanical behavior of the inclusions at the scale of the REV, which is viewed as a polycrystal. Hill's incremental inclusion-matrix interaction law relates the increments of stress and strain at the inclusion scale (noted $\delta\sigma_\alpha$ and $\delta\epsilon_\alpha$ respectively for inclusion α) to the increments of stress and strain at the REV scale (noted $\delta\bar{\sigma}$ and $\delta\bar{\epsilon}$ respectively), as follows:

$$\delta\sigma_\alpha - \delta\bar{\sigma} = -L^*(\delta\epsilon_\alpha - \delta\bar{\epsilon}) - \delta L^*(\epsilon_\alpha - \bar{\epsilon}) \quad (19)$$

where L^* is Hill's tensor, which depends on the shape of the inclusion and on the stiffness of the matrix. In the self-consistent method, the matrix is made of the assembly of inclusions present in the REV, and therefore, the stiffness of the matrix is not known *a priori*. Therefore, the resolution of Eq. (19) is iterative. Note that the stress and strain fields in each inclusion are assumed to be uniform, i.e. we assume that pressure-solution produces uniform changes of stress and strain in the hollow spherical inclusion. Since we present simulations done with uniform distributions of inclusion orientations, the matrix is isotropic. For spherical inclusions embedded in an isotropic matrix, Hill's tensor is expressed as (Hill, 1965; Eshelby, 1957):

$$L^*_{ijkl} = \frac{\mu^*}{4-5\nu}\left[(3-5\nu)\delta_{ij}\delta_{kl} + \frac{7-5\nu}{2}\left(\delta_{ik}\delta_{jl} + \delta_{il}\delta_{jk}\right)\right] \quad (20)$$

where ν is the Poisson's ratio of the matrix, and μ^* is the shear modulus of the matrix.

In porous media, it was shown that the shear modulus increases with the hydrostatic increment of stress (Digby, 1981). Moreover, the shear modulus depends on porosity (Kováčik, 2008). Accordingly, we choose an inclusion constitutive model that reflects a linear dependence of the shear and bulk moduli of the matrix (μ^* and k^*) to the porosity of the REV (ϕ^*), and we express the shear modulus as follows:

$$\mu^* = (1-\phi^*)\mu_o\left(\frac{\bar{\sigma}_e}{\bar{\sigma}_o}\right)^n \quad (21)$$

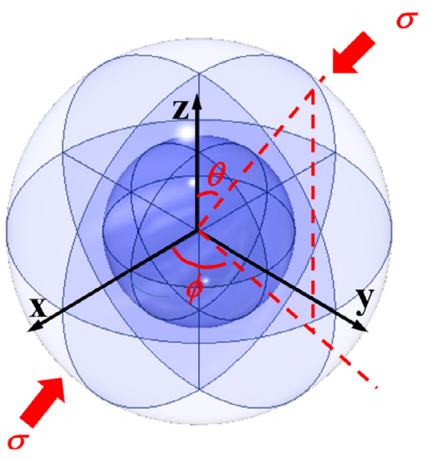

(a) Orientation of an inclusion

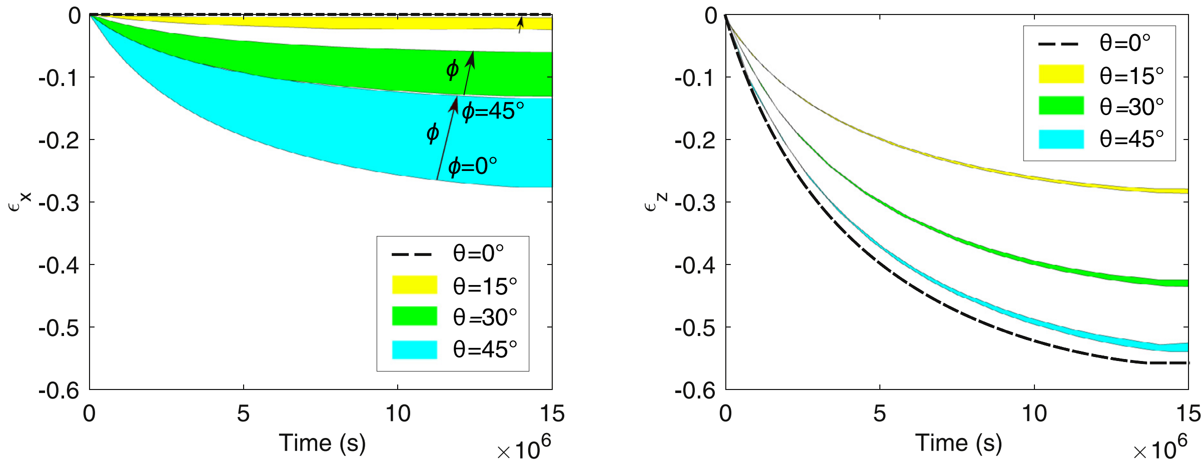

(b) ϵ_x vs. time

(c) ϵ_z vs. time

Fig. 8. Evolution of inclusion strains during a uniaxial creep test.

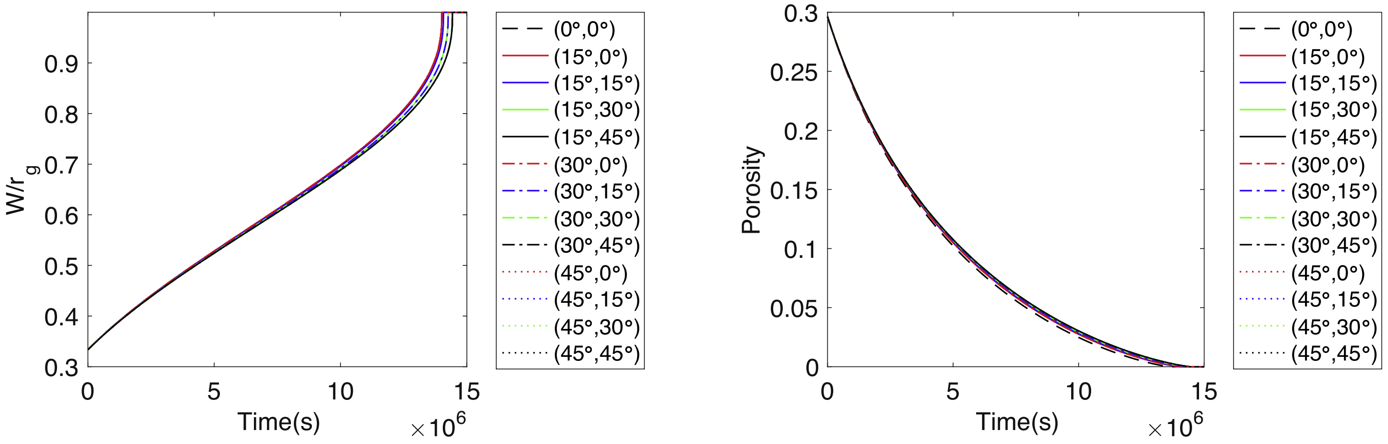

(a) Normalized wall thickness vs. time

(b) Porosity vs. time

Fig. 9. Evolution of inclusion geometry during a uniaxial creep test. Numbers into brackets indicate angular coordinates (θ, ϕ).

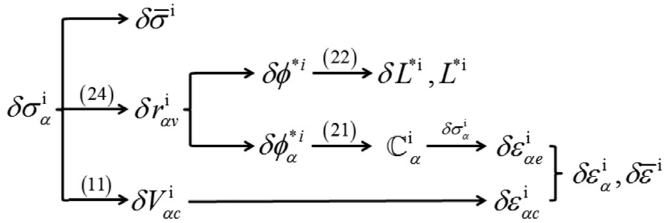

Fig. 10. Resolution algorithm with the proposed homogenization scheme.

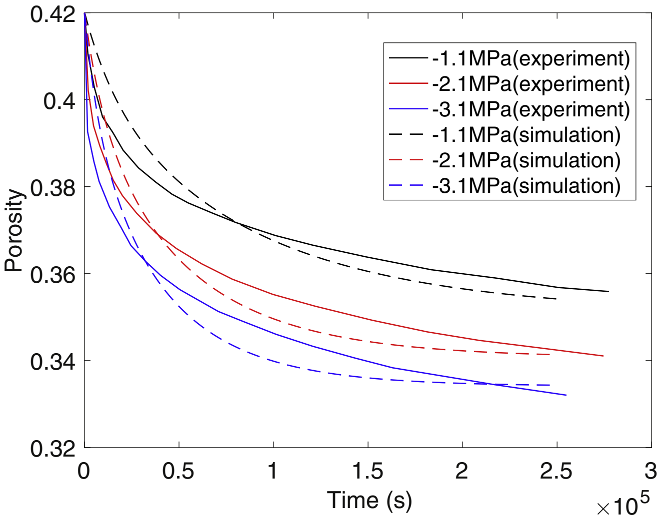

Fig. 11. Calibration of the model against uniaxial creep tests (tests under −2.1 MPa are used for verification).

where μ_o is the shear modulus of the solid part of the inclusion, and $\bar{\sigma}_e$ is the external global stress. $\bar{\sigma}_o$ and n are model parameters, that need to be calibrated. The decrease of REV porosity induces an increase of the matrix shear modulus μ^*, which results in a change of Hill's tensor L^*. We assume that the Poisson's ratio of the matrix (ν) is a material constant (Pouya et al., 2016). The incremental change of L^* can thus be expressed as:

$$\delta L^* = \frac{\partial L^*}{\partial \mu^*}\frac{\partial \mu^*}{\partial \phi^*}\delta\phi^* \tag{22}$$

3.3. Multi-scale chemical creep modeling

Following the self-consistent method, Eq. (19) is solved iteratively. At time step t_i, what is known from the previous time step t_{i-1} is: the REV stress $\bar{\sigma}^{i-1}$, the local stress of each inclusion, σ^{i-1}_α, the REV strain $\bar{\epsilon}^{i-1}$, the local strain of each inclusion, ϵ^{i-1}_α, the REV porosity ϕ^{*i-1}, the local porosity of each inclusion ϕ^{*i-1}_α, and the radius of the void in each inclusion, r^{i-1}_v. In the loading direction (z-axis), the REV axial stress at time t_i is known ($\bar{\sigma}^i_{zz}$ of known value in an oedometer test, $\delta\bar{\sigma}^i_{zz} = 0$ during a creep test). In oedometer tests and in uniaxial creep tests, the other boundary conditions imposed at time t_i are $\bar{\epsilon}^i_{xy} = 0$, $\bar{\epsilon}^i_{yz} = 0$, $\bar{\epsilon}^i_{xz} = 0$, $\bar{\epsilon}^i_{xx} = 0$ and $\bar{\epsilon}^i_{yy} = 0$. The variation of a local strain increment $\delta\epsilon^i_\alpha$ is the sum of the chemical strain increment, due to pressure solution (noted $\delta\epsilon^i_{\alpha c}$) and of the elastic local strain increment (noted $\delta\epsilon^i_{\alpha e}$). Thus the local stresses and strains in the inclusions can be obtained as follows:

$$\begin{aligned} &\delta\sigma^i_\alpha - \delta\bar{\sigma}^i + L^{*i}\left(\delta\epsilon^i_{\alpha c} + {\mathbb{C}^i_\alpha}^{-1} : \delta\sigma^i_\alpha - \delta\bar{\epsilon}^i\right) \\ &+ \delta L^{*i}\left(\epsilon^{i-1}_\alpha + \delta\epsilon^i_{\alpha c} + {\mathbb{C}^i_\alpha}^{-1} : \delta\sigma^i_\alpha - \bar{\epsilon}^{i-1} - \delta\bar{\epsilon}^i\right) = 0 \end{aligned} \tag{23}$$

By definition, the REV stress increment $\delta\bar{\sigma}^i$ (respectively the REV strain increment $\delta\bar{\epsilon}^i$) is the average of the local stress increments $\delta\sigma^i_\alpha$ (respectively the average of the local strain increments $\delta\epsilon^i_\alpha$). Using the expression of the dissolution velocity on each contact plane, the local chemical strain increment is obtained by calculating the change of inclusion radius induced by pressure solution under local stress σ^i_α and local stress change $\delta\sigma^i_\alpha$, according to the inclusion model explained in Eqs. (11)–(14). Now considering that the void inside the spherical inclusion remains a sphere upon pressure solution, the void radius $r_{\alpha v}$ is updated over time by using Eq. (15), as follows:

$$\delta r^i_{\alpha v} = -\frac{\dot{V}^i_{XY} + \dot{V}^i_{YZ} + \dot{V}^i_{XZ}}{A^{i-1}_s}\delta t \tag{24}$$

After updating the external radius and the pore radius in each inclusion, the variation of local porosity $\delta\phi^{*i}_\alpha$ and the variation of global porosity $\delta\phi^{*i}$ can be obtained, and the Hill's tensor is updated: δL^{*i}, L^{*i} are calculated according to Eq. (20)–(22). The porosity damage model employed at the REV scale is also used at the scale of the inclusion, so that the local stiffness tensor $\mathbb{C}^i_\alpha$ is replaced by $(1 - \Phi_\alpha)\mathbb{C}^i_\alpha$. The local elastic strain increment $\delta\epsilon^i_{\alpha e}$ is then calculated as the product of the inverse of the local stiffness matrix ${\mathbb{C}^i_\alpha}^{-1}$ by the local stress increment, $\delta\sigma^i_\alpha$. The algorithm is explained in the flow chart given in Fig. 10. All the unknown variables at time t_i in Eq. (23) can be regarded as functions of $\delta\sigma^i_\alpha$. Thus, six components of $\delta\sigma^i_\alpha$ are unknown for each inclusion, and Eq. (23) provides six equations.

Noting n the number of inclusions in the REV, $6n$ equations have to be solved for $6n$ unknowns at each time step. The Broyden-Fletcher-Goldfarb-Shanno (BFGS) algorithm (Fletcher, 1987; Lewis and Michael, 2008) is employed to solve this system of $6n$ implicit equations. We initialize stress by solving static mechanical balance equations, valid before pressure solution starts. According to Eq. (19), the corresponding increment of local stress is:

$$\delta\sigma^0_\alpha = \left(I + \mathbf{L}^{*0}{\mathbb{C}^0_\alpha}^{-1}\right)^{-1}\left(\delta\bar{\sigma}^0 + \mathbf{L}^{*0}\delta\bar{\epsilon}^0\right) \tag{25}$$

The initial local stress σ_α is calculated as $\sigma^0_\alpha = \delta\sigma^0_\alpha$. The initial increment of local strain $\delta\epsilon^0_\alpha$ is purely elastic, so $\delta\epsilon^0_\alpha$ equals ${\mathbb{C}^0_\alpha}^{-1}\delta\sigma^0_\alpha$. The initial local strain ϵ_α is initialized as $\epsilon^0_\alpha = \delta\epsilon^0_\alpha$.

4. Model calibration against brine-saturated creep tests

4.1. Model calibration against salt rock creep tests

The volumetric strain curves obtained by Spiers for wet salt aggregates (Spiers and Brzesowsky, 1993) are used to calculate the evolution of brine-saturated halite porosity during uniaxial creep tests. Experimental results obtained under axial stresses of −1.1MPa and −3.1MPa are used for calibration. The calibrated model is then compared to the results obtained under an axial stress of −2.1MPa for verification. The REV is represented by 300 spherical inclusions. The orientations of the inclusions are uniformly distributed. Due to the geometric assumptions made in the model, the radius of the inclusion (r_g) increases with the radius of a salt grain. In order to simulate realistic halite microstructures, we consider that r_g is equal to the characteristic grain size. r_g is considered uniform in the REV, and equal to 0.1375 mm, according to the experimental data reported in (Spiers and Brzesowsky, 1993). The initial porosity was 42% in the experiments. Correspondingly, the mean void radius was found to be 0.103mm. Based on experimental observations (Van Genuchten, 1980; Arson and Pereira, 2013), we assumed a lognormal distribution for the void radius, with a variance of 0.0001 mm^2. The calibration results are presented in Fig. 11 and Table 2.

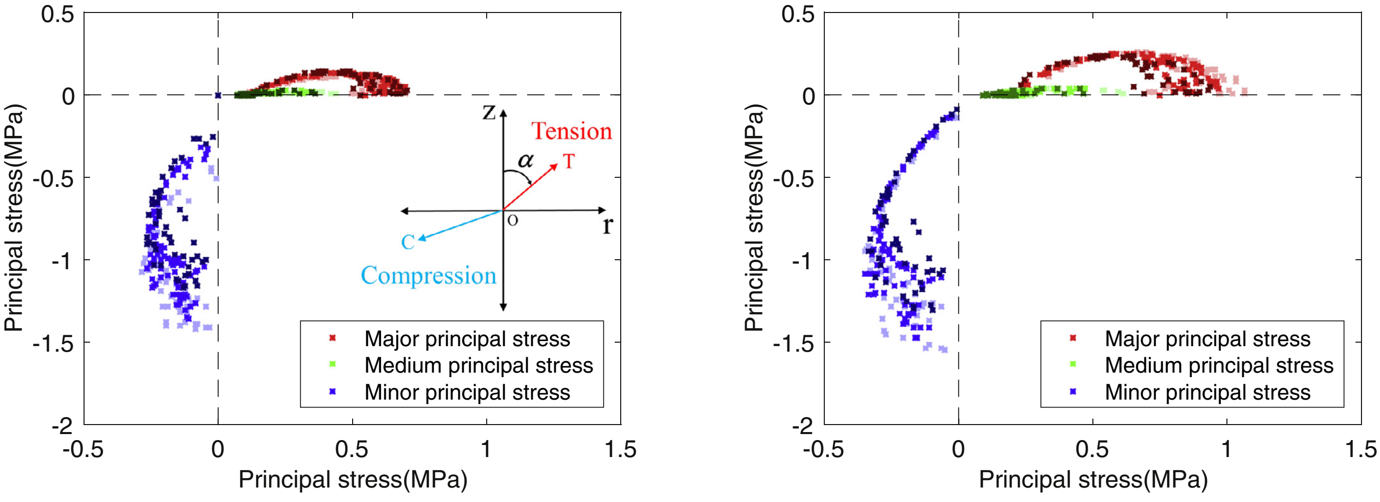

(a) Principal stresses at 100,000s

(b) Principal stresses at 250,000s

Fig. 12. Principal stresses in each inclusion, for a uniaxial creep test under −1.1 MPa.

Table 2
Model parameters found by calibration.

Elastic property		Chemical property
n	$\bar{\sigma}_o$	DS
–	MPa	mm^3/s
1.035	919	3.75×10^{-8}

Inclusions of different orientations or different initial void radius develop different microscopic principal stresses $\vec{\sigma}_p$. We represent the 300 minor, medium and major principal stresses on the map shown in Fig. 12(a): $\overrightarrow{OT}$ (in the upper right quadrant) represents a tensile principal stress, and $\overrightarrow{OC}$ (in the lower left quadrant) represents a compressive principal stress. α is the angle between the stress eigenvector and the orientation of the loading axis. The principal stresses in the 300 inclusions are shown for the test conducted under an axial stress of −1.1 MPa, after 100,000 s (27h40, Fig. 12(a)) and after 250,000 s (69h25, Fig. 12(b)). The dots with a lighter color represent inclusions with smaller initial voids.

According to Fig. 12, the major (tensile) principal stresses are almost perpendicular to the loading axis, while the minor (compressive) principal stresses tend to align with the loading direction. The magnitudes of the minor and major principal stresses increase with time. The minor principal stress is nearly zero in some inclusions, while it reaches a value close to −1.5 MPa in some other inclusions. Inclusions with larger initial voids tend to have smaller principal stresses. Fig. 13 illustrates the evolution local stress as a function of initial void radius and inclusion orientation for 10 representative inclusions. Fig. 13(b) confirms that before creep starts, the initial state of stress is different in each inclusion, because the inclusions considered have different initial void sizes. After 250,000 s, the state of stress is stable in each inclusion. Higher the initial stress, higher the healing rate, lower the final inclusion porosity. The compressive principal stress increases in magnitude with time for inclusions with small voids, while it decreases for inclusions with large voids. The final compressive principal stress is largely influenced by θ. If θ is close to 0° or 90°, small compressive principal stress is observed.

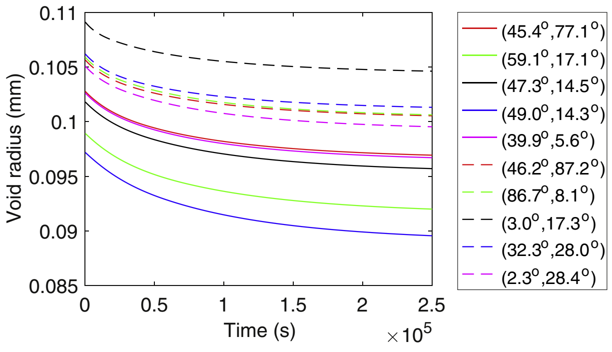

(a) Void radius vs. time

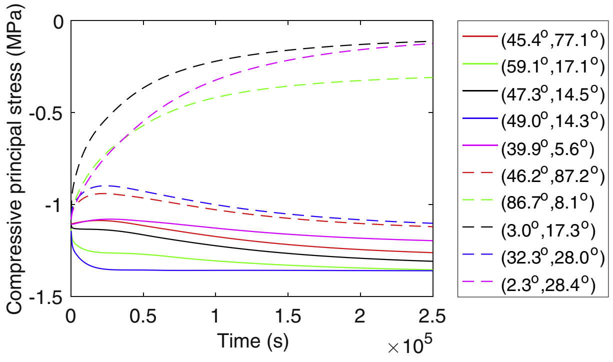

(b) Principal stress vs. time

Fig. 13. Evolution of the void radius and of the minor compressive principal stress in 10 different inclusions during the creep test performed under an axial load of -1.1 MPa. Numbers into brackets indicate angular coordinates (θ,ϕ). Dash lines refer to inclusions with large voids; solid lines refer to inclusion with small voids.

4.2. Sensitivity of the micro-macro model to the number of inclusions

Sensitivity analyses are performed to determine the minimum number of inclusions necessary to form a REV. We calibrate our model against oedometer tests performed under axial stresses of −1.1 MPa and −3.1 MPa, for a REV that contains 400 inclusions.

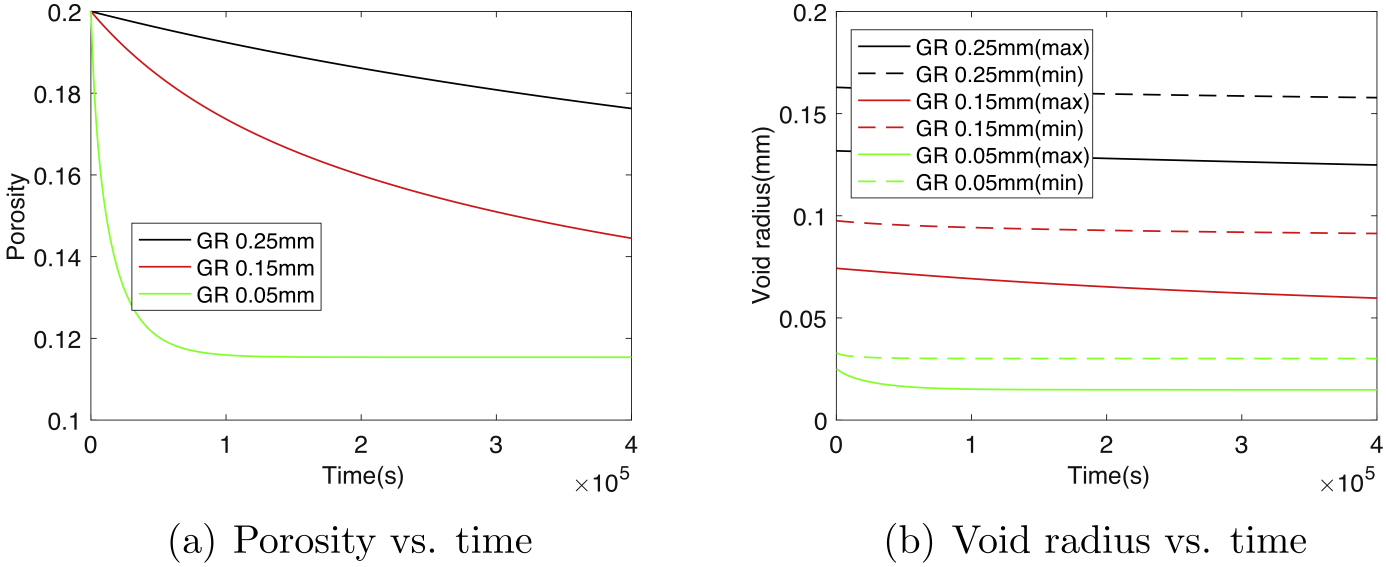

(a) Porosity vs. time (b) Void radius vs. time

Fig. 14. Influence of grain size on the healing rate.

Table 3
Error made on the estimation of the final porosity, compared to the porosity estimated with 400 inclusions.

Number of cells	50	100	200	300
Error (−1.1 MPa)	0.62%	0.96%	0.23%	0.26%
Error (−3.1 MPa)	1.34%	1.16%	1.00%	0.02%

We use the same distributions of orientations, porosity and size as in Section 4.1. The calibrated parameters are used to simulate the oedometer tests for REVs that contain less inclusions, and we find the minimum number of inclusions needed to match the results obtained with 400 inclusions with an acceptable error. Results are presented in Table 3. The error made on the estimation of the final porosity is less than 1.00% if the number of inclusions is at least 200. This finding validates the model calibration presented in Section 4.1 for 300 inclusions, and indicates that a set of 200 inclusions forms a REV. In the following, we present simulations done with REVs of 200 inclusions.

5. Influence of salt fabric on the healing rate and micro-macro creep behavior

In the following, we simulate a uniaxial oedometer creep test under -1.1MPa for REVs that contain 200 uniformly oriented inclusions. We study the sensitivity of the micro-macro model of chemo-mechanical healing to the microstructure of the polycrystal. The reference case is such that r_g is equal to 0.15 mm, the initial porosity of the REV is 20%, and the coefficient of variance (COV) of the void radius distribution is 0.05. Sensitivity analyses are performed for different values of r_g (0.05 mm, 0.25 mm), initial porosities (10%, 40%) and void radius COV (0.01, 0.1).

5.1. Influence of initial inclusion size

The rate of halite densification is known to be highly dependent on salt grain size. There are less inter-granular contact planes in the REV if salt crystals are larger. When salt polycrystals are saturated with brine, the size of salt grains not only affects the contact area between grains, but also controls the length of the diffusion path. Fig. 14 shows the variations of porosity and void radius with r_g during the oedometer test, with the reference REV inital porosity and void radius COV.

As could be expected from Eq. (11), a smaller inclusion radius leads to a larger dissolution rate at the grain boundaries, hence a faster healing rate. Results presented in Fig. 14(a) confirm this trend: a smaller grain size results in a faster rate of porosity decrease. It is interesting to note that porosity stabilizes to a nonzero value. This is because over time, the macroscopic stress is sustained by less and less inclusions: the inclusions under low stress undergo pressure solution at a negligible rate, and therefore, the full healing time cannot be reached during the simulation. Correspondingly, the void size distribution departs more and more from the initial uniform size distribution. This phenomenon is particularly visible for samples with smaller grains, see Fig. 14(b). When the initial grain radius is 0.05 mm, a minimum void radius is reached, beyond which no further healing is observed. Fig. 15 shows the microscopic principal stresses in the inclusions, for the three different grain sizes. All the principal stresses are initially compressive, because an oedometer test is simulated. Then, the major principal stress increases. For small grain sizes, the major and minor principal stresses are widely distributed and the rotation of the principal stresses is significant. Principal stresses do not evolve much once the REV porosity becomes stable.

5.2. Influence of initial porosity

Due to its high solubility, salt is easily dissolved in water. Larger void volume in salt rock usually results in lower stiffness and preferential fluid flow paths. Here, we study the effect of the initial porosity on the deformation of the brine-saturated halite polycrystal. Fig. 16 shows the variations of porosity and void radius with the initial REV porosity during the oedometer test, with the reference grain size and void radius COV. After 4×10^5 s (4 days and 15 h), the decrease in total porosity is about 5% in all cases. Under same initial void radius COV, void size heterogeneity increases with the initial porosity. In heterogeneous samples, smaller voids heal fast, and larger voids do not heal, which leads to a non-uniform healing rate over time. For smaller initial porosity, we observe a uniform healing rate. Fig. 17 shows the effect of initial porosity on the distribution of principal stresses in the inclusions. For higher initial porosity, we observe higher major tensile stresses, lower minor compressive stresses and a more significant rotation of principal stress directions over time. For the specimen with the lowest initial porosity, the major tensile principal stress increases rapidly

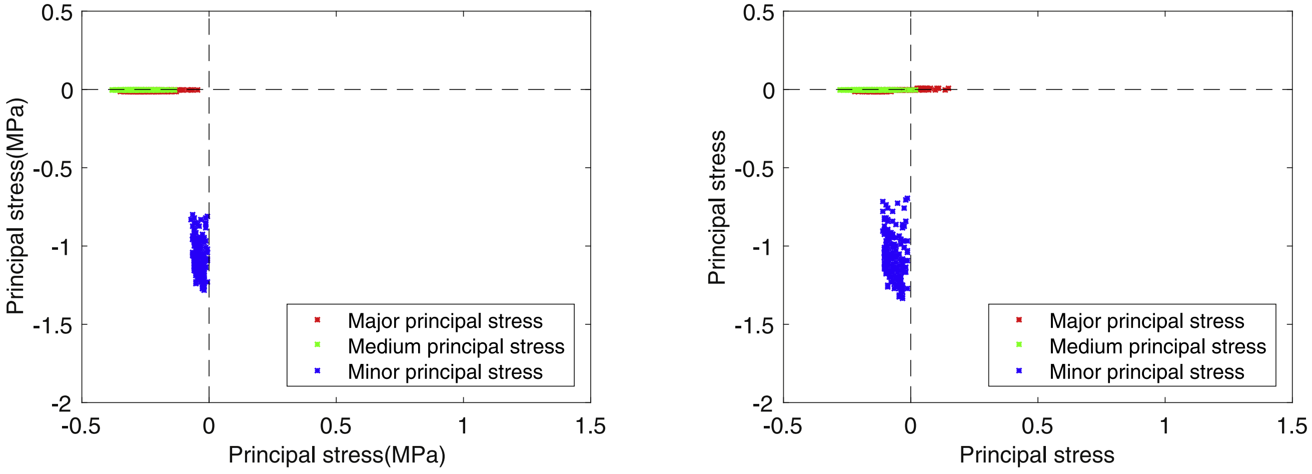

(a) After 2.3 days; r_g=0.25mm (b) After 4.6 days; r_g=0.25mm

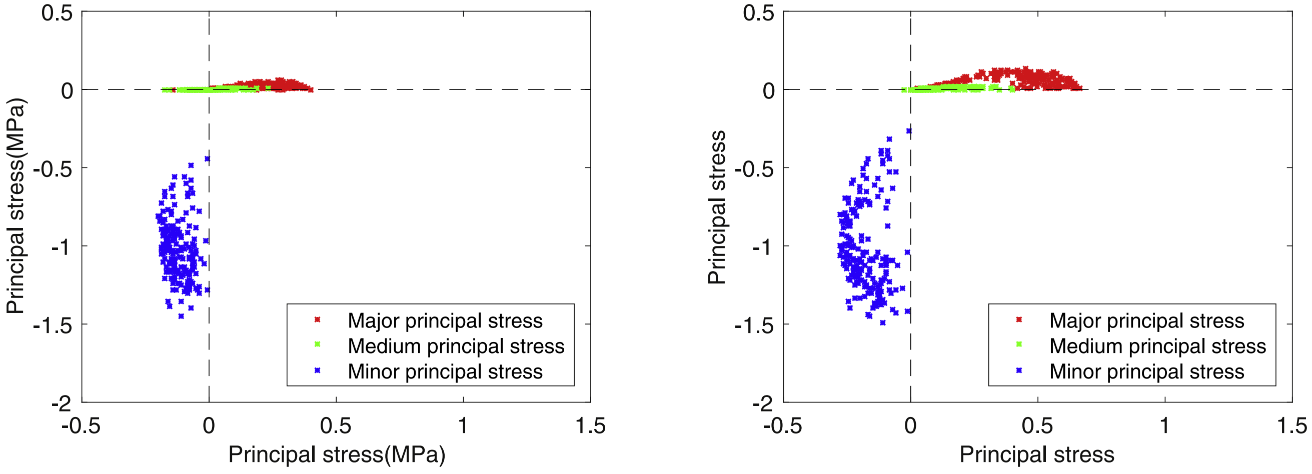

(c) After 2.3 days; r_g=0.15mm (d) After 4.6 days; r_g=0.15mm

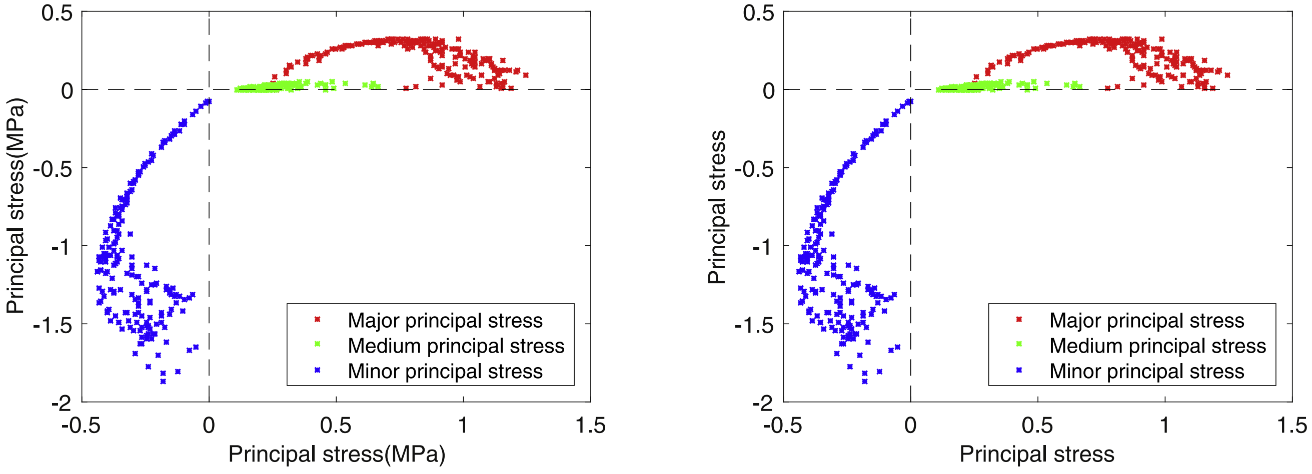

(e) After 2.3 days; r_g=0.05mm (f) After 4.6 days; r_g=0.05mm

Fig. 15. Principal stresses obtained during an oedometer test, for different grain sizes.

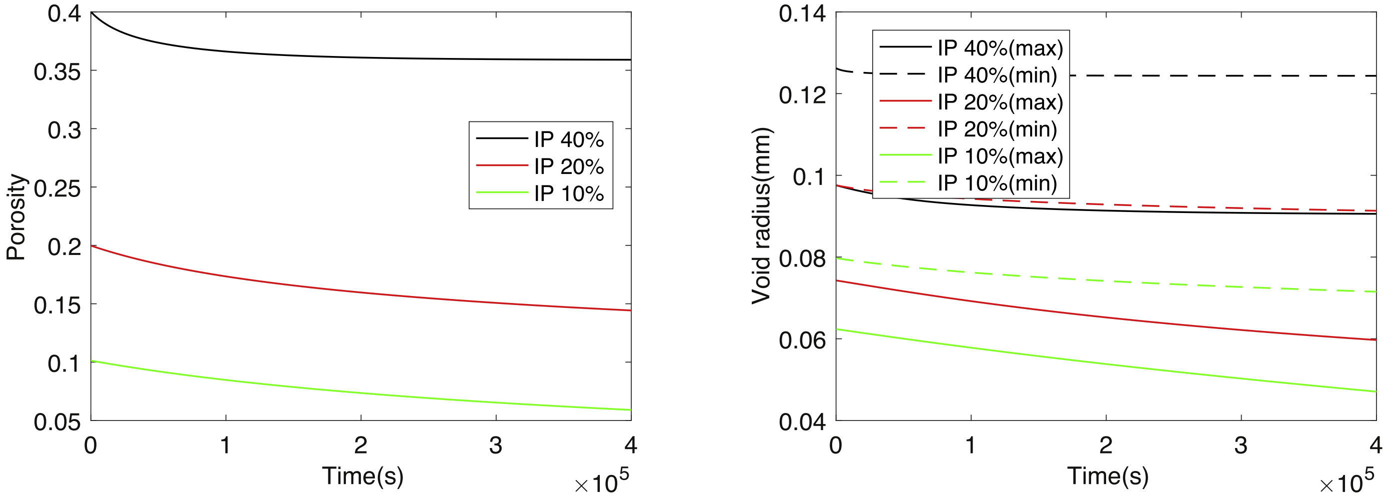

(a) Porosity vs. time (b) Void radius vs. time

Fig. 16. Effect of initial porosity on the evolution of porosity and void radius.

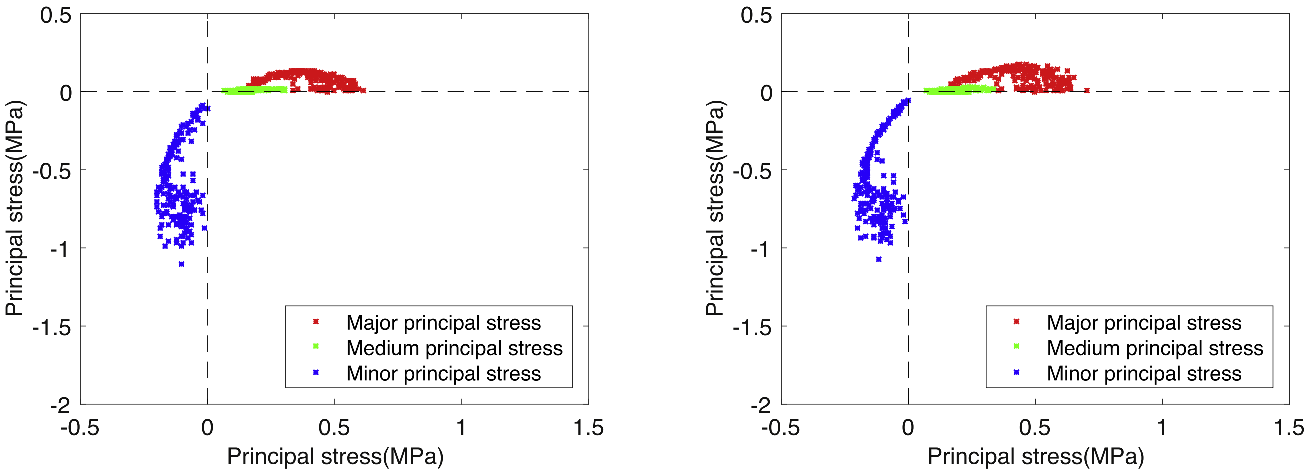

(a) After 2.3 days, initial porosity of 40% (b) After 4.6 days, initial porosity of 40%

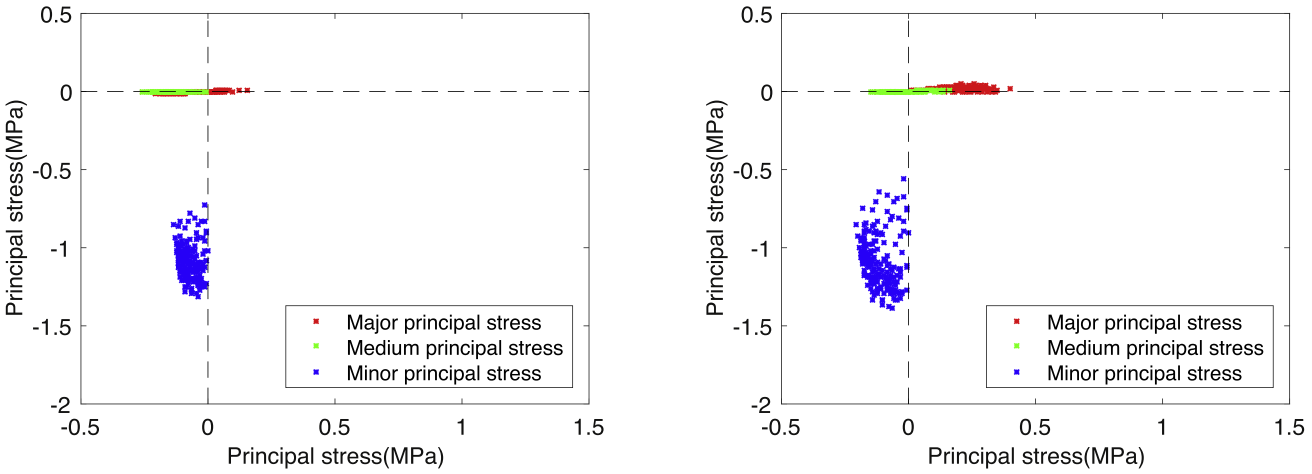

(c) After 2.3 days, initial porosity of 10% (d) After 4.6 days, initial porosity of 10%

Fig. 17. Evolution of principal stresses in the inclusions for different initial porosities.

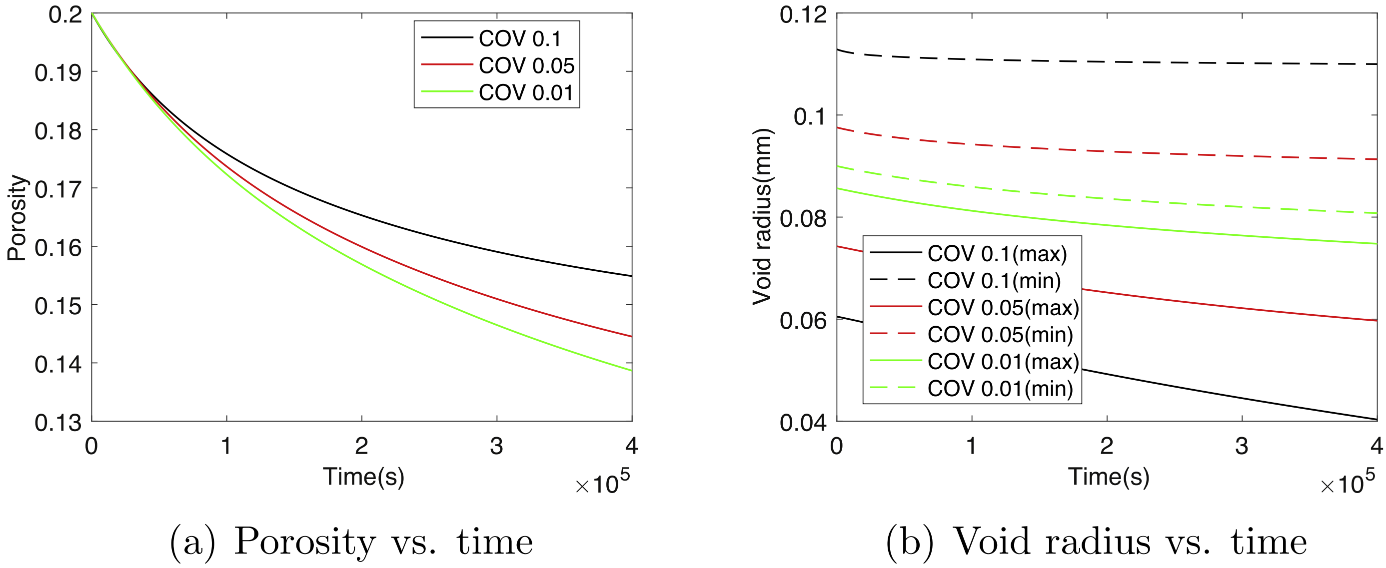

(a) Porosity vs. time (b) Void radius vs. time

Fig. 18. Influence of the void radius COV on the healing rate.

over time, in the radial direction, while the minor compressive stress remains stable.

5.3. Influence of the variance of the initial void radius distribution

Fig. 18 shows the variations of porosity and void radius with the void radius COV during the oedometer test, with the reference grain size and initial REV porosity.

According to Fig. 18(a), the rate of porosity change decreases when the void radius COV increases. This can be explained by the fact that the stiffness of inclusions increases when the void size decreases. As a result, inclusions with small voids undergo higher microscopic compressive stress, and heal faster. As healing proceeds in the inclusions that contain smaller pores, the void radius COV increases, which enhances the difference of healing rate between inclusions that contain small pores and inclusions that contain larger pores (Fig. 18(b)). Inclusions with large voids never heal completely, which slows down the overall healing rate of the REV. As expected, the distribution of principal stresses is more uniform in a sample that has a smaller void radius COV, see Fig. 19. Larger tensile stresses and compressive stresses are observed under small void size COV, as shown in Fig. 19. For larger void size COV, lower healing rates result in less stress redistribution and smaller tensile stresses and compressive stresses.

6. Conclusion

We present a chemo-mechanical self-consistent homogenization scheme for self-healing polycrystals. The model can be used to predict the evolution of stress, strain, porosity and stiffness at both micro- and macro-scales. The inclusion is a hollow sphere that contains a spherical void located at the intersection of three orthogonal grain-to-grain contact planes. Under compressive stress normal to any of those planes, the solid part of the inclusion dissolves. The solute diffuses towards the pore within the intergranular film, and precipitates at the pore wall. The resulting changes in the dimensions of the inclusion are used to calculate the viscous strain rate of the inclusion. The healing rate decreases over time. Sensitivity analyses performed at the inclusion scale under isotropic compressive stress indicate that the healing rate is higher under higher confining stress. Simulations of uniaxial creep tests show that the healing rate increases significantly when the component of compressive stress normal to the grain-to-grain contact plane is increased. Hill's inclusion-matrix interaction law is used to upscale strains and stresses at the REV scale. Oedometer tests were simulated for specimens containing spherical inclusions with uniformly distributed contact plane orientations. The REV porosity decreased at a decreasing rate in all cases. Inclusions with smaller voids are stiffer, and undergo higher compressive stress. As a result, it was observed that in samples containing inclusions with different initial void sizes, inclusions with larger voids had a negligible healing rate, and were slowing down the overall healing rate of the REV. In samples with uniformly distributed void sizes, the healing rate was faster, because all inclusions contributed to the healing of the REV. As expected, at the inclusion scale, major tensile stresses were mostly radial, and minor compressive stresses were mostly axial. In specimens with smaller grain sizes, principal stresses were more widely distributed in magnitude and the healing rate was higher. For uniform void size distributions, the healing rate increased with initial porosity, but the final porosity change did not depend on the initial porosity of the sample. Principal stresses of higher magnitude were noted in the inclusions that were part of REVs of high initial porosity.

Chemical reactions typically initiate at the location of microstructure defects, which would be very difficult to account for in a homogenization scheme that separates the solid and the pore phases, as is classically the case. The key here is that the inclusion is not a grain, but rather, a space that contains a pore and discontinuities, where chemical processes take place. Mass and energy balance equations are rigorously established to predict the chemical eigenstrain of each inclusion, which, added to the elastic deformation, provides the microstrain of each inclusion. From there, it is possible to use a matrix/inclusion interaction law to predict the mechanical response of a polycrystal subject to pressure solution under mechanical loading. The model was calibrated against experimental results published in the literature. Self-healing predictions are in agreement with physical observations. The proposed homogenization method paves the way to many future developments for upscaling chemo-mechanical processes in heterogeneous media. In addition, results obtained in this paper can guide the design of self-healing materials. For instance, a lower grain size promotes healing, whereas non-uniform void size distributions decelerate healing. Important lessons learnt in this study also concern the risk of grain (or crystal) breakage. For instance, larger

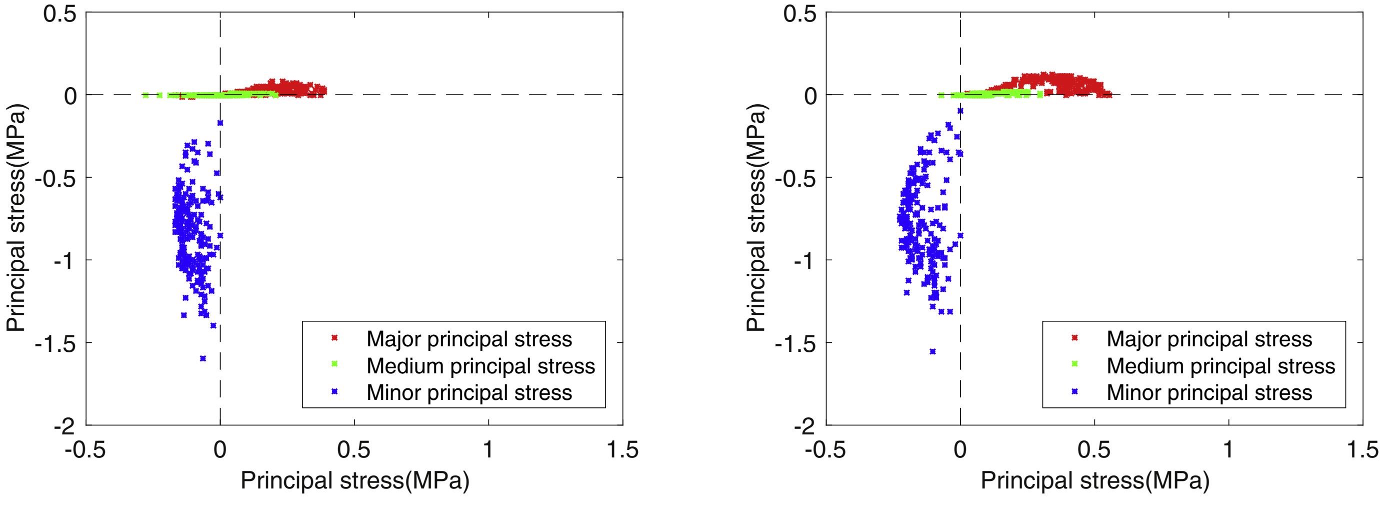

(a) After 2.3 days, COV=0.1

(b) After 4.6 days, COV=0.1

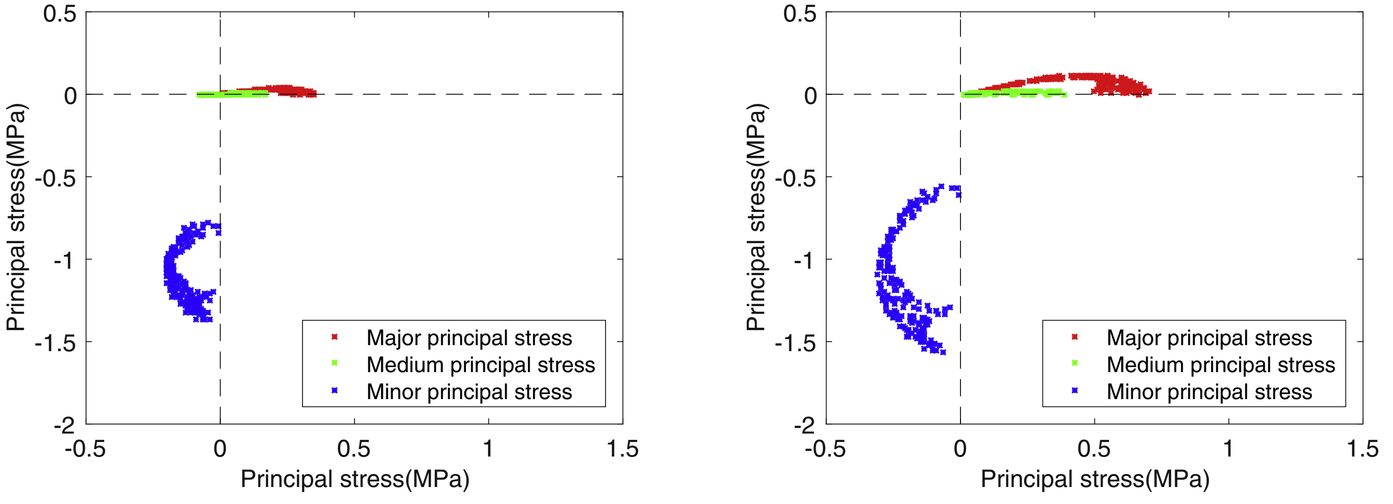

(c) After 2.3 days, COV=0.01

(d) After 4.6 days, COV=0.01

Fig. 19. Influence of void radius COV on the evolution of inclusion principal stresses.

microscopic stresses are noted in samples of high porosity, and in heterogeneous microstructures, grains that are close to smaller voids undergo higher stress. The paper focused on the coupled chemo-mechanical processes that occur at micro and macro scales to explain pressure-solution driven healing. In future work, we will study healing -induced anisotropy and accommodation, and we will extend the model to visco-plasticity under high stress conditions.

Acknowledgments

This research was supported by the U.S. National Science Foundation (grant CMMI#1552368: CAREER: Multiphysics Damage and Healing of Rocks for Performance Enhancement of Geo-Storage Systems – A Bottom-Up Research and Education Approach).

References

Al-Rub, R.K.A., Darabi, M.K., Little, D.N., Masad, E.A., 2010. A micro-damage healing model that improves prediction of fatigue life in asphalt mixes. Int. J. Eng. Sci. 48 (11), 966–990. Special Issue in Honor of K.R. Rajagopal. 10.1016/j.ijengsci.2010.09.016.

Arson, C., Pereira, J.-M., 2013. Influence of damage on pore size distribution and permeability of rocks. Int. J. Numer. Anal. Methods Geomech. 37 (8), 810–831.

Arson, C., Vanorio, T., 2015. Chemomechanical evolution of pore space in carbonate microstructures upon dissolution: linking pore geometry to bulk elasticity. J. Geophys. Res.: Solid Earth 120 (10), 6878–6894.

Barbero, E.J., Greco, F., Lonetti, P., 2005. Continuum damage-healing mechanics with application to self-healing composites. Int. J. Damage Mech. 14 (1), 51–81. doi:10.1177/1056789505045928.

Benveniste, Y., 1987. A new approach to the application of Mori-Tanaka's theory in composite materials. Mech. Mater. 6 (2), 147–157. doi:10.1016/0167-6636(87)90005-6.

Bourcier, M., Bornert, M., Dimanov, A., Héripré, E., Raphanel, J.L., 2013. Multiscale experimental investigation of crystal plasticity and grain boundary sliding in synthetic halite using digital image correlation. J. Geophys. Res.: Solid Earth 118 (2), 511–526. doi:10.1002/jgrb.50065.

Brantley, S.L., Kubicki, J.D., White, A.F., 2008. Kinetics of water-rock interaction, 168. Springer.

Castañeda, P., Willis, J., 1995. The effect of spatial distribution on the effective behavior of composite materials and cracked media. J. Mech. Phys. Solids 43 (12), 1919–1951. doi:10.1016/0022-5096(95)00058-Q.

Davies, R., Jefferson, A., 2017. Micromechanical modelling of self-healing cementitious materials. Int. J. Solids Struct. 113–114 (Supplement C), 180–191. doi:10.1016/j.ijsolstr.2017.02.008.

Digby, P., 1981. The effective elastic moduli of porous granular rocks. J. Appl. Mech. 48 (4), 803–808.

Eshelby, J.D., 1957. The determination of the elastic field of an ellipsoidal inclusion, and related problems. Proc. R. Soc. Lond. A: Math. Phys. Eng. Sci. 241 (1226), 376–396. doi:10.1098/rspa.1957.0133.

Fletcher, R., 1987. Practical methods of optimization. Wiley-interscience publication. Wiley.

Gardner, D., Jefferson, A., Hoffman, A., Lark, R., 2014. Simulation of the capillary flow of an autonomic healing agent in discrete cracks in cementitious materials. Cem. Concr. Res. 58 (Supplement C), 35–44. doi:10.1016/j.cemconres.2014.01.005.

Hickman, S.H., Evans, B., 1991. Experimental pressure solution in halite: the effect of grain/interphase boundary structure. J. Geol. Soc. Lond. 148 (3), 549–560. doi:10.1144/gsjgs.148.3.0549.

Hill, R., 1965. Continuum micro-mechanics of elastoplastic polycrystals. J. Mech. Phys Solids 13 (2), 89–101. https://doi.org/10.1016/0022-5096(65)90023-2.

Holcomb, D.J., Zeuch, D.H., 1990. Modeling the consolidation of a porous aggregate of dry salt as isostatic hot pressing. J. Geophys. Res.: Solid Earth 95 (B10), 15611–15622. doi:10.1029/JB095iB10p15611.

Houben, M., ten Hove, A., Peach, C., Spiers, C., 2013. Crack healing in rocksalt via diffusion in adsorbed aqueous films: microphysical modelling versus experiments. Phys. Chem. Earth, Parts A/B/C 64 (Supplement C), 95–104. Coupled Physical and Chemical Transformations Affecting the Performance of GeoSystems. 10.1016/j.pce.2012.10.001.

Kováčik, J., 2008. Correlation between elastic modulus, shear modulus, Poisson's ratio and porosity in porous materials. Adv. Eng. Mater. 10 (3), 250–252. doi:10.1002/adem.200700266.

Kröner, E., 1961. Zur plastischen verformung des vielkristalls. Acta Metall. 9 (2), 155–161. doi:10.1016/0001-6160(61)90060-8.

Lehner, F.K., 1990. Thermodynamics of rock deformation by pressure solution. Springer Netherlands, Dordrecht, pp. 296–333.

Lehner, F.K., 1995. A model for intergranular pressure solution in open systems. Tectonophysics 245 (3–4), 153–170.

Lewis, A. S., Michael, L. O., 2008. Nonsmooth optimization via bfgs.

Li, G., Uppu, N., 2010. Shape memory polymer based self-healing syntactic foam: 3-d confined thermomechanical characterization. Compos. Sci. Technol. 70 (9), 1419–1427. doi:10.1016/j.compscitech.2010.04.026.

McCLAY, K.R., 1977. Pressure solution and coble creep in rocks and minerals: a review. J. Geol. Soc. London 134 (1), 57. doi:10.1144/gsjgs.134.1.0057.

Mergheim, J., Steinmann, P., 2013. Phenomenological modelling of self-healing polymers based on integrated healing agents. Comput. Mech. 52 (3), 681–692. doi:10.1007/s00466-013-0840-0.

Miao, S., Wang, M.L., Schreyer, H.L., 1995. Constitutive models for healing of materials with application to compaction of crushed rock salt. J. Eng. Mech. 121 (10), 1122–1129.

Mori, T., Tanaka, K., 1973. Average stress in matrix and average elastic energy of materials with misfitting inclusions. Acta Metall. 21 (5), 571–574. doi:10.1016/0001-6160(73)90064-3.

Moyne, C., Murad, M.A., 2002. Electro-chemo-mechanical couplings in swelling clays derived from a micro/macro-homogenization procedure. Int. J. Solids Struct. 39 (25), 6159–6190. doi:10.1016/S0020-7683(02)00461-4.

van Noort, R., Spiers, C.J., 2009. Kinetic effects of microscale plasticity at grain boundaries during pressure solution. J. Geophys. Res.: Solid Earth 114 (B3).

Paterson, M.S., 1973. Nonhydrostatic thermodynamics and its geologic applications. Rev. Geophys. 11 (2), 355–389. doi:10.1029/RG011i002p00355.

Pluymakers, A.M.H., Spiers, C.J., 2015. Compaction creep of simulated anhydrite fault gouge by pressure solution: theory v. experiments and implications for fault sealing. Geol. Soc. Lond. Special Publ. 409 (1), 107–124. doi:10.1144/SP409.6.

Pouya, A., Zhu, C., Arson, C., 2016. Micro–macro approach of salt viscous fatigue under cyclic loading. Mech. Mater. 93, 13–31.

Pouya, A., Zhu, C., Arson, C., 2017. Self-consistent micromechanical approach for damage accommodation in rock-like polycrystalline materials. Int. J. Damage Mech. 0 (0). 1056789517747665. 10.1177/1056789517747665.

Raj, R., 1982. Creep in polycrystalline aggregates by matter transport through a liquid phase. J. Geophys. Res.: Solid Earth 87 (B6), 4731–4739. doi:10.1029/JB087iB06p04731.

Rutter, E.H., 1983. Pressure solution in nature, theory and experiment. J. Geol. Soc. Lond. 140 (5), 725–740. doi:10.1144/gsjgs.140.5.0725.

Rutter, E.H., Elliott, D., 1976. The kinetics of rock deformation by pressure solution [and discussion]. Philos. Trans. R. Soc.Lond. Ser. A, Math. Phys. Sci. 283 (1312), 203–219.

Schutjens, P., Spiers, C., 1999. Intergranular pressure solution in nacl: grain-to-grain contact experiments under the optical microscope. Oil Gas Sci. Technol. 54 (6), 729–750.

Spiers, C., Brzesowsky, R., 1993. Densification behaviour of wet granular salt: theory versus experiment. In: Seventh Symposium on salt, 1, pp. 83–92.

Spiers, C., De Meer, S., Niemeijer, A., Zhang, X., 2003. Kinetics of rock deformation by pressure solution and the role of thin aqueous films. Front. Sci. Ser. 129–158.

Spiers, C.J., Schutjens, P.M.T.M., Brzesowsky, R.H., Peach, C.J., Liezenberg, J.L., Zwart, H.J., 1990. Experimental determination of constitutive parameters governing creep of rocksalt by pressure solution. Geol. Soc. Lond. Spec. Publ. 54 (1), 215–227. doi:10.1144/GSL.SP.1990.054.01.21.

Urai, J.L., Spiers, C.J., Zwart, H.J., Lister, G.S., 1986. Weakening of rock salt by water during long-term creep. Nature 324 (6097), 554.

Van Genuchten, M.T., 1980. A closed-form equation for predicting the hydraulic conductivity of unsaturated soils. Soil Sci. Soc. Am. J. 44 (5), 892–898.

Voyiadjis, G.Z., Shojaei, A., Li, G., 2011. A thermodynamic consistent damage and healing model for self healing materials. Int. J. Plast. 27 (7), 1025–1044. doi:10.1016/j.ijplas.2010.11.002.

Voyiadjis, G.Z., Shojaei, A., Li, G., Kattan, P., 2012. Continuum damage-healing mechanics with introduction to new healing variables. Int. J. Damage Mech. 21 (3), 391–414. doi:10.1177/1056789510397069.

Weng, G., 1982. A unified, self-consistent theory for the plastic-creep deformation of metals. ASME Trans. J. Appl. Mech. 49, 728–734.

Wheeler, J., 2010. Anisotropic rheology during grain boundary diffusion creep and its relation to grain rotation, grain boundary sliding and superplasticity. Philos. Mag. 90 (21), 2841–2864.

White, S.R., Sottos, N., Geubelle, P., Moore, J., Kessler, M., Sriram, S., Brown, E., Viswanathan, S., 2001. Autonomic healing of polymer composites. Nature 409 (6822), 794–797.

Yang, C., Daemen, J., Yin, J.-H., 1999. Experimental investigation of creep behavior of salt rock. Int. J. Rock Mech. Min. Sci. 36 (2), 233–242. doi:10.1016/S0148-9062(98)00187-9.

Zhang, X., Spiers, C., 2005. Compaction of granular calcite by pressure solution at room temperature and effects of pore fluid chemistry. Int. J. Rock Mech. Min. Sci. 42 (7), 950–960. Rock Physics and Geomechanics. 10.1016/j.ijrmms.2005.05.017.

Zhu, C., Arson, C., 2015. A model of damage and healing coupling halite thermo-mechanical behavior to microstructure evolution. Geotech. Geol. Eng. 33 (2), 389–410. doi:10.1007/s10706-014-9797-9.